Electroluminescence and Photoluminescence Characterization of Multijunction Solar Cells

Helmut Nesswetter, Paolo Lugli, *Fellow, IEEE*, Andreas W. Bett, and Claus G. Zimmermann

***Abstract*—A combined electroluminescence and photoluminescence setup for a fast, nondestructive, and high-resolution characterization of large-area lattice matched $GaInP_2$/Ga(In)As/Ge triple-junction space solar cells was developed. In contrast with electroluminescence, where coupling effects between the subcells appear, all subcells can be analyzed independently in photoluminescence imaging, using three monochromatic light sources. This will be demonstrated by way of example for a partly irradiated cell. Alternatively, electroluminescence combined with simulation program with integrated circuit emphasis network simulations constitutes a powerful tool to extract quantitative information despite the coupling effects. Sheet resistances and shunts in individual subcells can be accurately modeled with this method.**

***Index Terms*—Electroluminescence, multijunction solar cell, photoluminescence, sheet resistance, shunt characterization, simulation program with integrated circuit emphasis (SPICE).**

I. Introduction

ELECTROLUMINESCENCE (EL) and photoluminescence (PL) measurements have emerged as an increasingly valuable tool predominantly for the characterization of silicon solar cells. Important solar cell parameters, like the minority carrier lifetime, diffusion length or series resistance, can be determined with high spatial resolution [1]. An imaging technique based on EL or PL is, in contrast with other characterization tools, which also offer spatial resolution, very fast and nondestructive. Luminescence imaging can also be applied straightforwardly to Cu(In,Ga)Se_2 [2] and polymer solar cells [3].

In contrast with these terrestrial cells, high-efficiency cells for space are multijunction cells. Currently lattice-matched $GaInP_2$/Ga(In)As/Ge triple-junction solar cells are state of the art in this application. The electrical and optical coupling of the individual subcells presents a set of new challenges in luminescence imaging. EL imaging is a fast and low-cost technique for detecting mechanical defects on large area space solar cells [4]. In addition, there are some first quantitative EL analyses on triple-junction solar cells based on the reciprocity relation [5]–[8]. The main potential of luminescence characterization of multijunction devices is the possibility to determine parameters of individual subcells. It is used for measuring the internal voltages of the subcells without spatial resolution [6], [7] and for a performance mapping of large area space cells [8]. Due to the fact that the subcells are electrically connected in series, inhomogenities, i.e., local shunts in one subcell, have influence on the current distribution and thus on the biasing conditions of each subcell. Combining EL with simulation program with integrated circuit emphasis (SPICE) network simulations is a suitable way to extract cell parameters quantitatively, like the sheet resistance and the magnitude of local shunts.

In PL, in contrast, each subcell can be excited homogenously provided that every excitation light source is only absorbed in one subcell, and suitable optics provide constant illumination over the complete cell area. For the characterization of multijunction solar cells PL is thus a very useful method to analyze single subcells independently. As an example, radiation-induced degradation can be resolved for the individual subcells.

II. Theory

The theoretical basis for EL imaging of solar cells is laid out in [5]. The reciprocity relation connects the spectral EL intensity φ_{EL} with the black body radiation, the external quantum efficiency EQE, and an exponential dependence of the voltage drop V over the pn-junction:

$$\varphi_{\mathrm{EL}}(E) = A \cdot E^2 e^{-\frac{E}{kT}} \mathrm{EQE}(E) e^{\frac{eV}{kT}} \tag{1}$$

with the photon energy E, summarized detector parameters A, and k, T and e have the usual meaning. Typically, bandpass filters for the complete EL peak are utilized in EL imaging, which results in an integrated intensity Φ_{EL}:

$$\Phi_{\mathrm{EL}} = \int \varphi_{\mathrm{EL}}(E) dE = C \cdot e^{\frac{eV}{kT}}$$

$$C = \int A \cdot E^2 e^{-\frac{E}{kT}} \mathrm{EQE}(E) dE. \tag{2}$$

The fundamental process for PL is spontaneous radiative recombination of excess charge carriers that are generated due to illumination. The rate of this radiative recombination is exponentially dependent on the splitting of the quasifermi levels and results in an exponential dependence on the diode voltage as well [9]:

$$\Phi_{\mathrm{PL}} \propto e^{\frac{eV}{kT}}. \tag{3}$$

Manuscript received May 21, 2012; revised July 9, 2012; accepted August 3, 2012. Date of publication September 20, 2012; date of current version December 19, 2012.

H. Nesswetter is with the Solar Array Center, EADS Astrium, 81663 Munich, Germany, and also with the Institute for Nanoelectronics, Technical University of Munich, 80333 Munich, Germany (e-mail: helmut.nesswetter@astrium.eads.net).

P. Lugli is with the Institute for Nanoelectronics, Technical University of Munich, 80333 Munich, Germany (e-mail: lugli@nano.ei.tum.de).

A. W. Bett is with the Fraunhofer Institute for Solar Energy Systems ISE, 79110 Freiburg, Germany (e-mail: andreas.bett@ise.fraunhofer.de).

C. G. Zimmermann is with the Solar Array Center, EADS Astrium, 81663 Munich, Germany (e-mail: claus.zimmermann@astrium.eads.net).

Color versions of one or more of the figures in this paper are available online at http://ieeexplore.ieee.org.

Digital Object Identifier 10.1109/JPHOTOV.2012.2213801

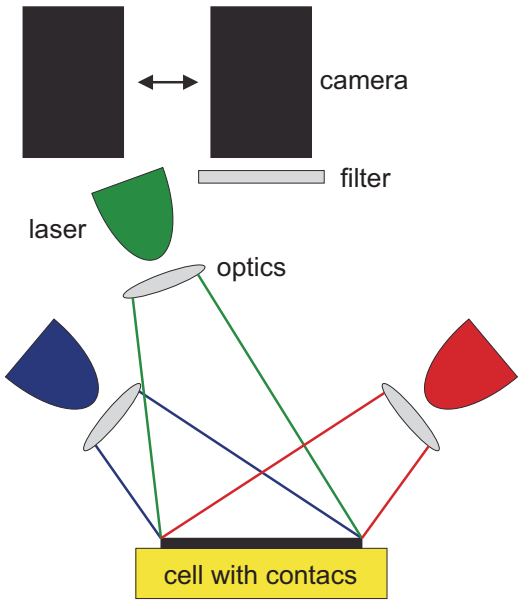

Fig. 1. Schematic illustration of the EL/PL setup. The key elements are two movable cameras equipped with suitable filters, three independent excitation light sources with custom optics, and the electrically contacted solar cell.

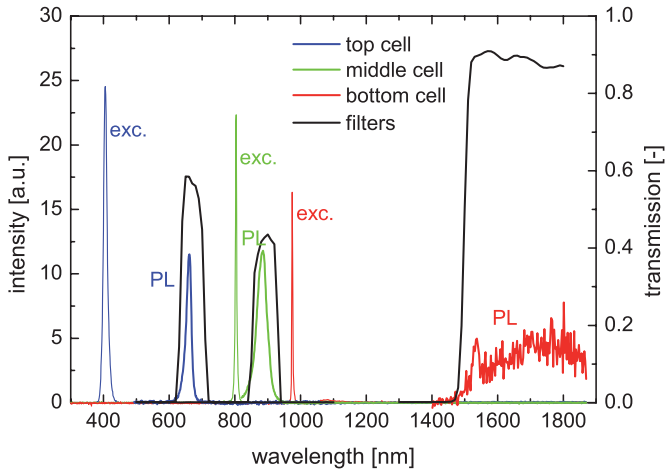

Fig. 2. Excitation (exc.) spectrum of the setup combined with the PL spectrum of a triple-junction cell. The excitation wavelength for the top cell at 405 nm and its luminescence peak at 660 nm are highlighted in blue. The corresponding excitation/luminescence peaks are shown in green for the middle cell at 803 nm/885 nm and in red at 975 and 1700 nm for the bottom cell. The black curves denote the transmission curves of the three corresponding bandpass filters used.

Consequently for both, EL and PL, there is an exponential dependence of the luminescence intensity on the diode voltage. Therefore, a luminescence image primarily yields information of the voltage distribution over the cell area.

III. Setup

Fig. 1 shows a schematic of the combined EL and PL setup. The cell is placed on a temperature controlled vacuum chuck. For EL measurements, a four-quadrant sourcemeter is used to forward bias the cell. It can also act as a current sink during illumination.

For the PL illumination three independent light sources are installed. The $GaInP_2$ top cell can be excited with a 405 nm LED array, the Ga(In)As middle cell with a 803 nm diode laser and the Ge bottom cell with a 975 nm diode laser. In front of each light source, a specially designed lens array ensures a homogeneous illumination of the whole cell area, typically 8×4 cm^2, under the inclined illumination conditions. All three light sources are spatially aligned for a simultaneous illumination of all subcells. The luminescence images for top and middle cell are acquired with a Si CCD camera. A second CCD camera with a HgCdTe sensor is used for the bottom cell. The cameras are mounted on a rail so that they can be moved automatically atop the subcell of interest. Dielectric filters in front of the camera lens ensure that only luminescence from the subcell of interest is detected and that scattered light from the excitation light sources is blocked. The spectrum in Fig. 2 illustrates the excitation light sources together with the corresponding luminescence peaks and the transmission curves of the three filters. Due to the indirect bandgap in germanium, the bottom cell luminescence peak is much lower and noisier in comparison with top and middle cells.

IV. Spice Network Model

For a theoretical analysis of the voltage distribution of the individual subcells, a cross-connected 3-D network model is solved with a SPICE. Specifically, LTSpice IV from Linear Technology Corporation is used [10]. Similar SPICE network models are already applied to single-junction GaAs solar cells [11], [12], to thin film Cu(In,Ga)Se_2 solar modules [13], as well as to III–V triple-junction solar cells [14], [15]. Except for [13], all these models have in common that these are tailored to concentrator solar cells with a relatively small size, and their main focus is on the electrical performance under concentrated sunlight. For the modeling of EL images, performed at orders of magnitude lower injection currents, different simplifications apply. In particular, vertical resistances like the contact resistance between the frontside metallization and the semiconductor material can be neglected, whereas current-spreading effects and thus lateral resistances become much more important.

In the network model, the cell area is divided into individual pixels, where each pixel consists of a stack of diodes. A section of the equivalent circuit is shown in Fig. 3. The typical size of the simulated pixels is 130×130 μm^2, which results in 10 pixels between two gridfingers. The diode properties of each pixel are assumed identical. Because of computational limitations, it is not possible to simulate the whole 30 cm^2 cell area with this spatial resolution. In contrast with [13] which uses a variable adaptive mesh in the following simulations only a fraction of interest, typically 1 cm^2 is simulated, and it is implicitly assumed that the current density in this area is the same as in the whole solar cell.

The electrical behavior of the individual pn-junctions is derived from dark *I–V* curves of the corresponding component cells that consist of the same semiconductor materials, but have only one active pn-junction. Based on these dark *I–V* curves, a two-diode model for the top and middle cell had to be used, whereas

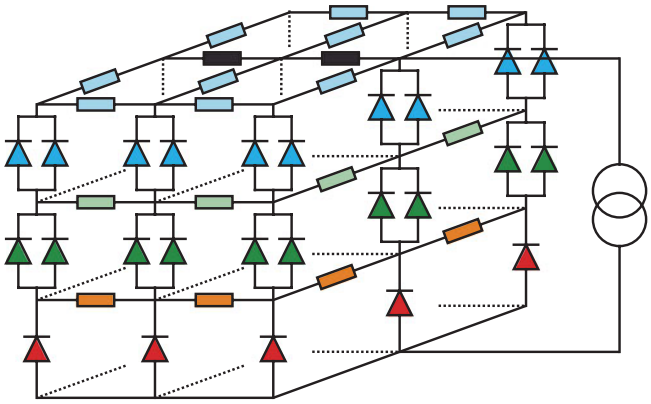

Fig. 3. Part of the 3-D SPICE network model for EL simulations. The pairs of two diodes for the top (blue) and middle cells (green) in series with the bottom cell diode (red) are interconnected with ohmic resistances. The black resistance elements on top represent a gridfinger to which an external current source is connected.

TABLE I
PARAMETERS OF THE SPICE MODEL

Subcell	Parameter
top	J_{01} = 1.4E-27 A/cm^2
	n_{top1} = 1
	J_{02} = 2.8E-12 A/cm^2
	n_{top2} = 2.93
	R_{top} = 600 Ω/□*
middle	J_{01} = 3.1E-19 A/cm^2
	n_{mid1} = 1
	J_{02} = 6.0E-11 A/cm^2
	n_{mid2} = 2
	R_{mid} = 100 Ω/□*
bottom	J_0 = 1.9E-6 A/cm^2
	n_{bot} = 1.13
	R_{bot} = 2000 Ω/□*

*See Section V-B.

for the bottom cell a standard one-diode model proved to be sufficient. In contrast with the model from Steiner *et al.* [14], tunneling diodes are neglected in the equivalent circuit, since the current densities in EL measurements are orders of magnitude lower than in concentrator solar cells.

The ohmic resistances of the silver frontside metallization are calculated from the specific resistance of silver and the geometrical dimensions of the gridfingers. The interconnections between neighboring stacks via ohmic resistances are especially important at local inhomogenities. One resistance element in the network combines the sheet resistances of all layers in between two pn-junctions. For example, the resistance R_{mid} between top and middle cells is a parallel connection of the top cell base and back surface field layers, the two layers of the tunneling junction and the window and emitter layer of the middle cell. The resistance values for a typical cell structure are mentioned in [4]. They are the main parameters that are adjusted to the experiment. All parameters for the SPICE model are listed in Table I.

A current source is connected between the common back contact and the front. A common front contact that interconnects all parallel gridfingers is neglected. The end points of all gridfingers are rather assumed to be at the same potential and are thus connected to the current source directly.

The SPICE simulation results in the electrical potential and current at every node. In particular, the voltage drop across each diode can be calculated. Using (2) a luminescence image for a certain temperature can be derived straightforwardly. The constant C in (2) is dependent on the local cell temperature, the local EQE near the bandgap and the local filter transmission curve next to camera parameters like the integration time. Since these values are difficult to obtain, the value for C is adjusted for one pixel, typically located in a valley between two gridfingers. This way the correlation between the SPICE voltage data and the luminescence intensities is achieved. The same C is then used for all remaining pixels in the simulation.

V. Experimental and Simulation Results

A. Qualitative Differences of EL and PL Imaging for Multijunction Solar Cells

There are some fundamental differences of EL and PL imaging when considering multijunction solar cells. Fig. 4 shows EL and PL images of all three subcells for a 4 × 4 cm^2 $GaInP_2$/Ga(In)As/Ge cell that has been partly irradiated with 1 MeV electrons. During irradiation, the main part of the cell was shielded with a 2 mm aluminum plate. Within the smaller circle of diameter 7.1 mm, the total dose was 1E15 e$^-$/cm^2, and within the larger circle of diameter 9.6 mm, it was 3E14 e$^-$/cm^2. In contrast with [16], it is not possible to analyze the luminescence spectrum because the camera detects the integrated intensity with respect to the filter transmission curve. However, the imaging technique provides a high spatial resolution, and shows the difference between irradiated and not irradiated areas on the same cell. To obtain some spectral information together with a high spatial resolution, narrow bandpass filters could be used.

According to [17], electron irradiation mainly affects the middle cell and the top cell to a lesser degree. The bottom cell is known to be very radiation hard especially in the wavelength range where the direct bandgap absorption contributes mostly to the photovoltaic effect [18]. This is in very good agreement with the PL images on the right-hand side of Fig. 4, where only top and middle cell images show the signature of the irradiation pattern. For the top cell, it is even visible that the higher dose in the small circle leads to lower V_{oc}, and thus a lower PL intensity than in that the large circle. The same holds true for the middle cell image, but due to the brightness and contrast settings it is not visible in the image. The bottom cell has a very homogeneous PL intensity even in the irradiated circles since the excitation wavelength of 975 nm is absorbed via the direct bandgap of germanium.

In contrast with the PL images, where the excitation is completely independent and homogeneous for each subcell, the EL images on the left-hand side of Fig. 4 show a completely

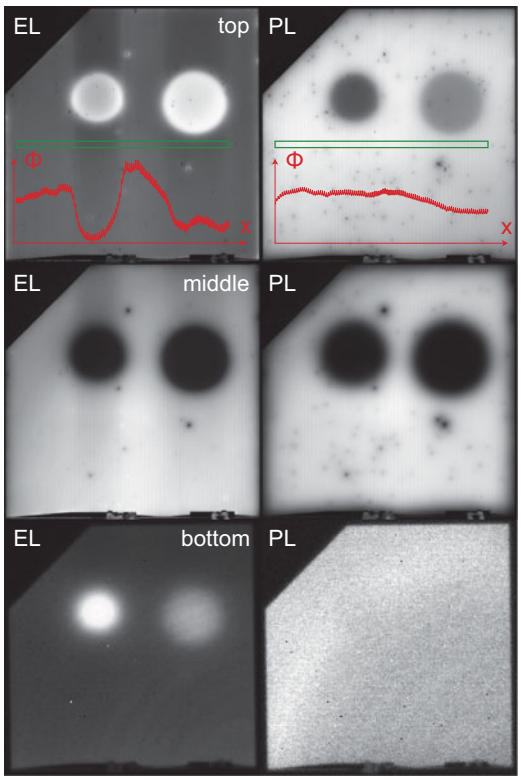

Fig. 4. EL and PL images of all three subcells of a 4 × 4 cm^2 partly electron irradiated solar cell. The small circle received 1E15 e^-/cm^2 and the large circle 3E14 e^-/cm^2. The red curves in the top cell images indicate the luminescence profile along the green line.

different intensity distribution for the top and bottom cells. Only the middle cell EL image looks similar to the PL one. Taking the degradation of EQE and (1) into account the EL intensity should be lower in the irradiated part of the top and middle cells, if the other parameters were homogeneous over the complete cell area. If series resistance effects are neglected, the external voltage drop over the complete triple-junction cell area is constant. The degradation of the *I–V* parameters mainly for the middle as well as for the top cell leads to an increased current density in the irradiated areas. This is confirmed by the bottom EL image that can be used as a simplified current map [8]: As evidenced by the PL image, the bottom cell *I–V* parameters are homogeneous. Therefore, the bright spots in the EL image, which are primarily due to an increased diode voltage, directly reflect a locally higher bottom cell current. For the top cell, the higher current density overcompensates the radiation-induced degradation, as well as leads to a higher voltage drop over the irradiated diodes.

Next to this electrical coupling of the three subcells series resistance effects are another difference of EL and PL imaging. The red curves in the top cell images of Fig. 4 show the luminescence profile across the cell below the irradiated parts. In the case of PL, it is approximately constant but in the EL case there is a decrease in intensity above and below the irradiated circles. The reason can be found in the ohmic resistance of the gridfingers, running in vertical direction. They are not clearly visible in Fig. 4 due to the high-density grid for this kind of cell. The higher current in gridfingers connected to the irradiated cell areas results in an increased voltage drop over the gridfinger itself. Therefore, the voltage at the pn-junctions is lower, and the EL intensity along those gridfingers decreases. The effect is also visible in the middle and the bottom EL images, but increasingly smeared out from the top to the bottom cell.

These qualitative differences of EL and PL imaging are fundamentally the same for a local shunt in one subcell, which also increases the local current density.

B. Sheet Resistance Determination With EL and SPICE

The sheet resistances of the different solar cell layers together with the ohmic resistance of the frontside metallization determine the overall series resistance and therefore have influence on the electrical performance of the entire solar cell. For luminescence imaging, the sheet resistances have a large impact on the surroundings of local inhomogenities, which are the source of lateral currents. This effect can also be exploited beneficially for the detection of mechanical defects [4]. In the SPICE model, in Section IV, all layers between two pn-junctions of a multijunction solar cell are combined in one lateral conducting layer with a certain ohmic resistance. For single-junction cells of $GaInP_2$ [19] and CIGS [20], there are already methods for determining the sheet resistance using spatially resolved EL. In these cases, the sheet resistance is calculated by solving a differential equation based on Ohm's law and the continuity equation.

When using no special test structure, the effect of sheet resistances for a conventional cell design is mainly visible in the EL profile between two gridfingers, at higher current densities, i.e., 33 mA/cm^2 and particularly in the top cell. To determine the sheet resistances for the middle and bottom cell as well, a part of the cell with a broken gridfinger is of advantage. In such a region, the influence of the sheet resistances is stronger. Fig. 5 shows the EL images for 33 mA/cm^2 in the left column together with SPICE simulations in the middle and the corresponding cross-sectional luminescence profiles in the right column.

The SPICE simulations are in very good agreement with the measurements if the ohmic resistances for the interconnection of neighboring diodes are adjusted. An increase in the simulated solar cell area has no influence on the results and therefore justifies the reduction of the simulation area to a part of the cell. In comparison with a similar cell structure mentioned in [4], the combined lateral resistance above the top cell is increased from 293 to 600 $\Omega/\square$ and the one between top and middle cells from 28 to 100 $\Omega/\square$. A large discrepancy is found for the lateral resistance between middle and bottom cells where the value has to be changed from 1.5 to 2000 $\Omega/\square$. The likely explanation presumably lies in the adapted device design with a modified nucleation layer. This leads to a lower conductivity within the nucleation layer itself. The diffused emitter of the bottom cell is thinner and lower doped, which also increases the lateral resistance. It has to be mentioned that for the simulation, the sheet resistance of overlaying lateral conducting layers has influence on the adjustment of the resistances below because it

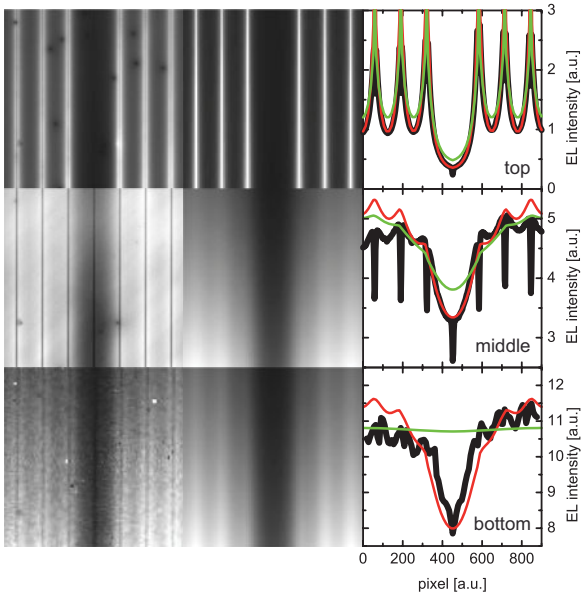

Fig. 5. EL measurements (left column) and corresponding SPICE simulations (middle column) at 33 mA/cm^2 for top, middle, and bottom cells. The right-hand column shows the measured (black) and simulated luminescence profiles for two sets of lateral resistances. The red curves are obtained for $R_{\mathrm{top}} = 600\,\Omega/\square$, $R_{\mathrm{mid}} = 100\,\Omega/\square$ and $R_{\mathrm{bot}} = 2000\,\Omega/\square$. They represent the best match and are those used in the SPICE EL maps in the middle column. The green profiles are obtained for $R_{\mathrm{top}} = 293\,\Omega/\square$, $R_{\mathrm{mid}} = 28\,\Omega/\square$, $R_{\mathrm{bot}} = 1.5\,\Omega/\square$.

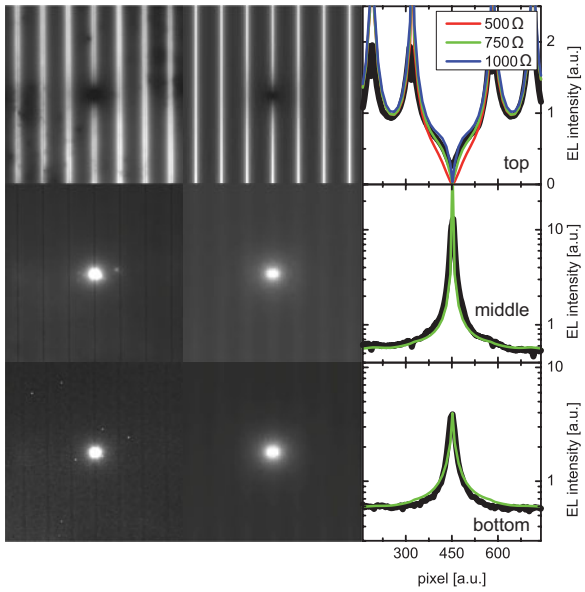

Fig. 6. EL measurements (left column) and corresponding SPICE simulations (middle column) at 33 mA/cm^2 with $R_{\mathrm{shunt}} = 750\ \Omega$ for top, middle, and bottom subcells. In the right column, the measured (black) luminescence profile in horizontal direction across the shunt together with the simulated ones for $R_{\mathrm{shunt}} = 500\ \Omega$ (red), $R_{\mathrm{shunt}} = 750\ \Omega$ (green), and $R_{\mathrm{shunt}} = 1000\ \Omega$ (blue) are shown.

defines the current injection in the subcell below. Consequently, the accuracy of the method is decreasing from top to bottom.

C. Quantitative Shunt Characterization With EL and SPICE

Prominent defects in triple-junction solar cells are local shunts in the top cell, which can be detected and analyzed with luminescence imaging. In [21], the different impacts of shunt resistance and sheet resistance for PL imaging of single-junction silicon solar cells are presented. Recently, also a PL-based method for a quantitative shunt calculation on silicon solar cells was proposed [22]. It requires either a PL image before the cell was shunted or it is assumed that the PL intensity would be homogeneous if there is no shunt. The combination of EL and SPICE is an alternative pathway to analyze shunts quantitatively.

In the left column of Fig. 6, the EL signature of a typical top shunt is shown at 33 mA/cm^2. The high current density is of advantage because of the fact that large area cells typically exhibit several shunts of different strength. In the simulation, only the strongest shunt with surroundings is modeled. The higher the current density in the measurement, the lower is the influence of the weaker shunts and they can be neglected.

Focused ion beam and transmission electron microscopy analysis of cells with equivalent top shunt EL signatures show that the defect size is in the order of some microns and, therefore, smaller than a single pixel. Its electrical impact, however, is much larger due to lateral currents. The shunt reduces the local diode voltages in a wide area and results in a dark spot on the top cell EL image. Electrical coupling equivalent to the partly irradiated cells in Section V-A causes the bright spots on the middle and bottom cell EL images.

The luminescence profiles across the top cell shunt are shown in the right column of Fig. 6. In order to introduce the shunt in the SPICE network, an ohmic resistance in parallel to the top cell diodes is introduced in one SPICE pixel directly underneath a gridfinger. The simulated top cell profiles are adjusted to the measurement profile by varying the absolute value of the shunt resistance, while the sheet resistances were fixed at the values determined before in Section V-B. The best match is found for 750 Ω, whereas 500 Ω and 1000 Ω do not provide a good match. Similar to the simulation of the broken gridfinger, there is no influence of the simulated cell area. As shown in the green curves of Fig. 6, this shunt resistance simultaneously leads to an excellent match of the EL profiles for the middle and bottom cell without further adjustments. Since they are also dependent on the shunt value and the sheet resistances, this match confirms not only the shunt resistance of 750 Ω, but also the sheet resistances from Section V-B.

VI. Summary

A combined setup for spatially resolved EL and PL characterization of large area $GaInP_2$/Ga(In)As/Ge triple-junction solar cells was presented. The differences of EL and PL imaging like electrical coupling and series resistance effects were highlighted using a partly electron irradiated solar cell. Furthermore, the potential of EL imaging in combination with SPICE network simulations for multijunction cells was shown. Sheet resistances and local defects can be characterized quantitatively.

REFERENCES

[1] T. Trupke, R. A. Bardos, M. D. Abbott, P. Würfel, E. Pink, Y. Augarten, F. W. Chen, K. Fisher, J. E. Cotter, M. Kasemann, M. Rüdiger, S. Kontermann, M. C. Schubert, M. The, S. W. Glunz, W. Warta, D. Macdonald, J. Tan, A. Cuevas, J. Bauer, R. Gupta, O. Breitenstein, T. Buonassisi, G. Tarnowski, A. Lorenz, H. P. Hartmann, D. H. Neuhaus, and J. M. Fernandez, "Progress with luminescence imaging for the characterization of silicon wafers and solar cells," in *Proc. 22nd Eur. Photovoltaic Sol. Energy Conf.*, 2007, pp. 22–31.

[2] T. Kirchartz and U. Rau, "Electroluminescence analysis of high efficiency Cu(In,Ga)Se2 solar cells," *J. Appl. Phys.*, vol. 102, pp. 104510-1–104510-8, 2007.

[3] M. Seeland, R. Rösch, and H. Hoppe, "Luminescence imaging of polymer solar cells: Visualization of progressing degradation," *J. Appl. Phys.*, vol. 109, pp. 064513-1–064513-5, 2011.

[4] C. G. Zimmermann, "Utilizing lateral current spreading in multijunction solar cells: An alternative approach to detecting mechanical defects," *J. Appl. Phys.*, vol. 100, pp. 023714-1–023714-8, 2006.

[5] U. Rau, "Reciprocity relation between photovoltaic quantum efficiency and electroluminescent emission of solar cells," *Phys. Rev. B*, vol. 76, pp. 085303-1–085303-8, 2007.

[6] R. Hoheisel, S. Rönsch, F. Dimroth, A. W. Bett, H. Nesswetter, and C. G. Zimmermann, "Electroluminescence exposes individual performances in multi-junction cells," *Compd. Semicond.*, vol. 17, pp. 28–31, 2011.

[7] T. Kirchartz, U. Rau, M. Hermele, A. W. Bett, A. Helbig, and J. H. Werner, "Internal voltages in GaInP/GaInAs/Ge multijunction solar cells determined by electroluminescence measurements," *Appl. Phys. Lett.*, vol. 92, pp. 123502-1–123502-3, 2008.

[8] C. G. Zimmermann, "Performance mapping of multijunction solar cells based on electroluminescence," *IEEE Electron Device Lett.*, vol. 30, no. 8, pp. 825–827, Aug. 2009.

[9] K. Schick, E. Daub, S. Finkbeiner, and P. Würfel, "Verification of a generalized planck law for luminescence radiation from silicon solar cells," *Appl. Phys. A: Mater. Sci. Process.*, vol. 54, pp. 109–114, 1992.

[10] (April 30, 2012). LTSpice IV. [Online]. "http://www.linear.com/designtools/software/

[11] M. Steiner, S. P. Phillipps, M. Hermele, A. W. Bett, and F. Dimroth, "Validated front contact grid simulations for GaAs solar cells under concentrated sunlight," *Prog. Photovoltaics Res. Appl.*, vol. 19, pp. 73–83, 2011.

[12] B. Galiana, C. Algora, I. Rey-Stolle, and I. G. Vara, "A 3-D model for concentrator solar cells based on distributed circuit units," *IEEE Trans. Electron Devices*, vol. 52, no. 12, pp. 2552–2558, Dec. 2005.

[13] B. Pieters, "Spatial modeling of thin-film solar modules using the network simulation method and SPICE," *IEEE J. Photovoltaics*, vol. 1, no. 1, pp. 93–98, Jul. 2011.

[14] M. Steiner, W. Guter, G. Peharz, S. P. Philipps, F. Dimroth, and A. W. Bett, "A validated SPICE network simulation study on improving tunnel diodes by introducing lateral conducting layers," *Prog. Photovoltaics Res. Appl.*, vol. 20, pp. 274–283, 2012.

[15] K. Nishioka, T. Takamoto, T. Agui, M. Kaneiwa, Y. Uraoka, and T. Fuyuki, "Evaluation of InGaP/InGaAs/Ge triple-junction solar cell under concentrated light by simulation program with integrated circuit emphasis," *Jpn. J. Appl. Phys.*, vol. 43, pp. 882–889, 2004.

[16] H. Sugimoto, M. Tajima, S. Hase, and M. Imaizumi, "Luminescence analysis of radiation effects in multijunction solar cells for space," in *Proc. 31st IEEE Photovoltaic Spec. Conf.*, Jan. 2005, pp. 830–833.

[17] C. Baur, M. Meusel, F. Dimroth, A. W. Bett, M. Nell, G. Strobel, S. Taylor, and C. Signorini, "Analysis of the radiation hardness of triple- and quintuple-junction space solar cells," in *Proc. 31st IEEE Photovoltaic Spec. Conf.*, Jan. 2005, pp. 548–551.

[18] R. Hoheisel, J. Fernandez, F. Dimroth, and A. W. Bett, "Investigation of radiation hardness of germanium photovoltaic cells," *IEEE Trans. Electron Devices*, vol. 57, no. 9, pp. 2190–2194, Sep. 2010.

[19] K. Xiong, W. He, S. Lu, T. Zhou, D. Jiang, R. Wang, K. Qiu, J. Dong, and H. Yang, "Analysis of lateral current spreading in solar cell devices by spatially-resolved electroluminescence," *J. Appl. Phys.*, vol. 107, pp. 124501-1–124505-6, 2010.

[20] M. Paire, L. Lombez, J. Guillemoles, and D. Lincot, "Measuring sheet resistance of CIGS solar cell's window layer by spatially resolved electroluminescence imaging," *Thin Solid Films*, vol. 519, pp. 7493–7496, 2011.

[21] M. Kasemann, D. Grote, B. Walter, W. Kwapil, T. Trupke, Y. Augarten, R. A. Bardos, and E. Pink, "Luminescence imaging for the detection of shunts on silicon solar cells," *Prog. Photovoltaics Res. Appl.*, vol. 16, pp. 297–305, 2008.

[22] Y. Augarten, T. Trupke, M. Lenio, J. Bauer, J. W. Weber, M. Juhl, M. Kasemann, and O. Breitenstein, "Calculation of quantitative shunt values using photoluminescence imaging," *Prog. Photovoltaics Res. Appl.,* [online]. Available: http://onlinelibrary.wiley.com/doi/10.1002/pip.2180/abstract;jsessionid=AB02AC89282FFB817F20AF9933367BD1.d01t04?systemMessage=Wiley+Online+Library+will+be+disrupted+on+15+September+from+10%3A00-12%3A00+BST+%2805%3A00-07%3A00+EDT%29+for+essential+maintenance&userIsAuthenticated=false&deniedAccessCustomisedMessage=

Authors' photographs and biographies not available at the time of publication.